JOURNAL OF GEOPHYSICAL RESEARCH, VOL. 103, NO. D24, PAGES 32,195–32,213, DECEMBER 27, 1998

Sensitivity of multiangle imaging to aerosol optical depth and to pure-particle size distribution and composition over ocean

Ralph Kahn, Pranab Banerjee, Duncan McDonald, and David J. Diner

Jet Propulsion Laboratory, California Institute of Technology, Pasadena

Abstract. Multiangle, multispectral remote sensing observations, such as those anticipated from the Earth Observing System (EOS) Multiangle Imaging Spectroradiometer (MISR), can significantly improve our ability to constrain aerosol properties from space. Simulations over cloud-free, calm ocean conditions were studied for pure particles with natural ranges of optical depth, particle size, and indices of refraction. According to the theoretical simulations we can retrieve column optical depth from measurements over calm ocean for all but the darkest particles, with typical size distributions and compositions, to an uncertainty of at most 0.05 or 20%, whichever is larger, even if the particle properties are poorly known. For one common particle type, soot, constraints on the optical depth over dark ocean are very poor. The simulated measurements also allow us to distinguish spherical from nonspherical particles, to separate two to four compositional groups based on indices of refraction, and to identify three to four distinct size groups between 0.1 and 2.0 μm characteristic radius at most latitudes. The technique is most sensitive to particle microphysical properties in the "accumulation mode" sizes, where particle scattering undergoes the transition from Rayleigh to large-particle regimes for the MISR wavelengths. On the basis of these results we expect to distinguish air masses containing different aerosol types, routinely and globally, with multiangle remote sensing data. Such data complement in situ and field data, which can provide detailed information about aerosol size and composition locally. An extension of this study to mixtures of pure particles is part of continuing work.

1. Introduction

Recent advances in modeling the Earth's climate have brought us to a point where the contributions made by aerosols to the global radiation budget significantly affect the results [e.g., *Andreae*, 1995; *Charlson et al.*, 1992; *Hansen et al.*, 1997; *Penner et al.*, 1994]. Aerosols are thought to contribute to direct radiative forcing in the atmosphere and, indirectly, through their influence as nucleation sites for cloud particles. Knowledge of both aerosol optical depth and the microphysical properties of particles is needed to adequately model aerosol effects.

Currently, we must rely on satellite remote sensing to provide the spatial and temporal coverage required for global monitoring of atmospheric aerosols. However, the retrieval of aerosol properties by remote sensing is a notoriously underdetermined problem, and the only operational, global-scale, satellite-based retrieval of aerosols derives aerosol optical depth from single-angle, monospectral data, using assumed values for all the aerosol microphysical properties [*Rao et al.*, 1989; *Stowe et al.*, 1997].

Multiangle, multispectral remote sensing observations, such as those anticipated from the Earth Observing System (EOS) Multiangle Imaging Spectroradiometer (MISR), provide a type of information about the characteristics of aerosols never before obtained from satellites [*Diner et al.*, 1991, 1998]. We plan to retrieve aerosol optical depth and aerosol "type," which represents a combination of index of refraction, size distribution, and shape constraints, globally, at 17.6-km spatial resolution.

MISR is scheduled for launch into polar orbit on the EOS-AM (ante meridiem) platform in late 1998 or early 1999. It will measure the upwelling visible radiance from Earth in four spectral bands centered at 446, 558, 672, and 866 nm, at each of nine view angles spread out in the forward and aft directions along the flight path at 70.5°, 60.0°, 45.6°, 26.1°, and nadir. The maximum spatial sampling rate is 275 m in the cross-track and along-track directions, at all angles except nadir, where the cross-track value is 250 m. Over a period of 7 min, a 360-km-wide swath of Earth comes into the view of the cameras at each of the nine emission angles, providing a wide range of scattering angle coverage for each surface location. The data will be used to characterize aerosol optical depth, aerosol type, surface albedo and bidirectional reflectance, and cloud properties. Complete coverage of latitude bands will take 9 days at the equator and 2 days in polar regions; the nominal mission lifetime is 6 years.

This is the second in a series of papers that explores our ability to retrieve information about atmospheric aerosols from MISR. The first paper [*Kahn et al.*, 1997] asks how well we can distinguish spherical from nonspherical particles having microphysical properties commonly associated with mineral dust from the Sahara desert. On the basis of theoretical simulations we showed that over calm ocean surfaces, and with expected ranges of particle optical depth and size distribution, MISR can distinguish spherical from nonspherical particles and can retrieve column optical depth for these nonspherical particles to an uncertainty of at most 0.05 or 20%, whichever is larger. At most latitudes, MISR can also identify three to four

Paper number 98JD01752.
0148-0227/98/98JD-01752$09.00

distinct size groups between 0.1 and 2.0 μm characteristic radius.

In this paper we expand this work to include natural ranges of optical depth, particle size distribution, and composition for common types of spherical particles. We concentrate on situations under which the MISR sensitivity to particle properties (except possibly absorption) is likely to be greatest: over calm ocean. These results provide a theoretical upper bound on the sensitivity of actual MISR retrievals for all aerosol properties except particle single scattering albedo, which may be better constrained over land surfaces with spatially varying contrast.

For this study we consider atmospheres containing "pure" particle types: aerosol populations with uniform composition and with aerosol sizes characterized by unimodal, lognormal distribution functions. A future paper will treat the MISR sensitivity to mixtures of particle types.

2. Our Approach to the Aerosol Sensitivity Study

Our overall approach is to designate one set of simulated reflectances as MISR "measurements," with an atmosphere having fixed aerosol optical depth (τ_a), particle characteristic radius (r_a), real index of refraction (nr_a), and imaginary index of refraction (ni_a). We then test whether they can be distinguished, within instrument uncertainty, from a series of "comparison" model reflectances. For the comparison models we systematically vary the four comparison model parameters: aerosol optical depth (τ_c), characteristic radius (r_c), real index of refraction (nr_c), and imaginary index of refraction (ni_c). The goal is to determine the ranges of comparison model properties that give an acceptable match with the measurements.

Prior to launch of the MISR instrument we rely on simulations of top-of-atmosphere radiation to explore the sensitivity of multiangle observations to aerosol properties. The MISR Team has developed a radiative transfer code, based on the adding-doubling method [*Hansen and Travis*, 1974], to simulate reflectances as would be observed by MISR for arbitrary choice of aerosol type and amount and variable surface reflectance properties [*Diner et al.*, 1997]. For the present study we simulated MISR measurements over a Fresnel-reflecting flat ocean surface in a cloud-free, Rayleigh scattering atmosphere with a surface pressure of 1.013 bars and a standard midlatitude temperature profile. (In the actual MISR retrievals over ocean, we model Sun glint and whitecaps, which depend on near-surface wind speed [*Martonchik et al.*, 1998].)

A layer containing particles with selected optical depth, spectral single scattering albedo, extinction coefficient, and single scattering phase function is placed between the gas component and the surface. (We assume here that the vertical distribution of aerosols has a negligible effect on the results. Our tests with particles inside and above the Rayleigh scattering layer show that particularly at the blue and green wavelengths and at the steepest emission angles the effect may be significant. However, atmospheric aerosols are usually concentrated near the surface, and the MISR dark water retrievals use only the red and infrared channels, for which Rayleigh scattering is small. In the actual MISR retrievals we will consider a "transported mineral dust" particle type that models desert dust advected high in the atmosphere.) Extinction and scattering properties for lognormal distributions of spherical particles are derived at selected values of particle characteristic radius (r_c), real index of refraction, and imaginary index of refraction, using a standard Mie scattering code. The lognormal function is given as

$$\text{lognormal}\,(r) = \frac{1}{r\,\ln(\sigma)\,\sqrt{2\pi}} \exp\left[-\frac{[\ln(r) - \ln(r_c)]^2}{2[\ln(\sigma)]^2}\right] \tag{1}$$

The width parameter (σ) in this function is set to 2.5 for accumulation, 2.0 for coarse, and 2.0 for nucleation modes, representing fairly broad, natural distributions of particles.

2.1. Testing the Agreement Between Comparison Models and "Measurements"

Over ocean, the MISR retrieval makes use of up to 18 measurements: nine angles at each of the two longest MISR wavelengths (bands 3 and 4, centered at 672 and 866 nm, respectively), where the water surface is darkest. We define four test variables to decide whether a comparison model is consistent with the measurements. Each is based on the χ^2 statistical formalism [e.g., *Bevington and Robinson*, 1992].

One test variable weights the contributions from each observed reflectance according to the slant path through the atmosphere of the observation:

$$\chi^2_{\mathrm{abs}} = \frac{1}{N\langle w_k\rangle} \sum_{l=3}^{4} \sum_{k=1}^{9} \frac{w_k[\rho_{\mathrm{meas}}(l,k) - \rho_{\mathrm{comp}}(l,k)]^2}{\sigma^2_{\mathrm{abs}}(l,k)} \tag{2}$$

where ρ_{meas} is the simulated "measurement" of atmospheric equivalent reflectance and ρ_{comp} is the simulated equivalent reflectance for the comparison model. (We define equivalent reflectance as the radiance multiplied by π and divided by the exoatmospheric solar irradiance at normal incidence.) The indices l and k are the indices for wavelength band and camera, N is the number of measurements included in the calculation, w_k are weights, chosen to be the inverse of the cosine of the emission angle appropriate to each camera k, $\langle w_k\rangle$ is the average of weights for all the measurements included in the summation, and σ_{abs} is the absolute calibration uncertainty in the equivalent reflectance for MISR band l and camera k. For MISR the nominal value of $\sigma_{\mathrm{abs}}/\rho$ falls between 0.03 for a target with equivalent reflectance of 100% and 0.06 for an equivalent reflectance of 5% in all channels [*Diner et al.*, 1997]. For the simulations we model σ_{abs} as varying linearly with equivalent reflectance (Figure 1).

The test variable χ^2_{abs} alone reduces 18 measurements to a single statistic, which emphasizes the absolute reflectance and depends heavily on aerosol optical depth for bright aerosols over a dark surface. However, there is more information in the measurements which we can use to improve the retrieval discrimination ability.

A second χ^2 test variable emphasizes the geometric properties of the scattering, which depend heavily on particle size and shape. The camera-to-camera relative uncertainty is small compared to the absolute uncertainty. The χ^2_{geom} test variable takes advantage of this fact; each spectral measurement is divided by the corresponding spectral measurement in the nadir camera:

$$\chi^2_{\mathrm{geom}} = \frac{1}{N\langle w_k\rangle} \sum_{l=3}^{4} \sum_{\substack{k=1 \\ k\neq \mathrm{nadir}}}^{9} \frac{w_k\left[\dfrac{\rho_{\mathrm{meas}}(l,k)}{\rho_{\mathrm{meas}}(l,\mathrm{nadir})} - \dfrac{\rho_{\mathrm{comp}}(l,k)}{\rho_{\mathrm{comp}}(l,\mathrm{nadir})}\right]^2}{\sigma^2_{\mathrm{geom}}(l,k)} \tag{3a}$$

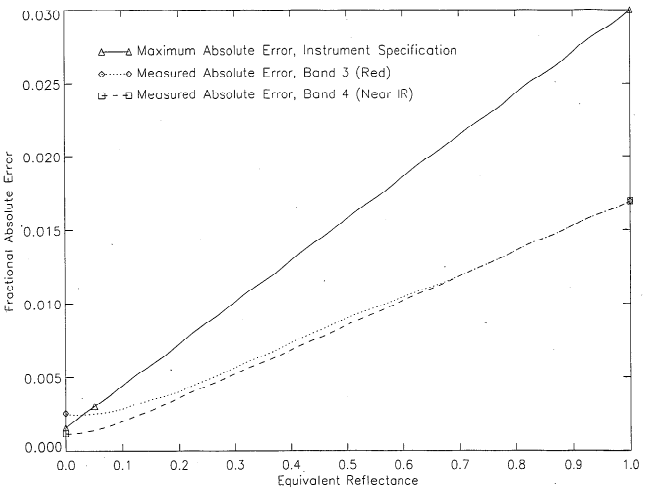

Figure 1. MISR absolute radiometric uncertainty assumed for this study, based on nominal instrument requirements [*Diner et al.*, 1997] and laboratory measurements [*Bruegge et al.*, 1998]. These curves are assumed to apply to all cameras. The relative band-to-band and camera-to-camera uncertainties are assumed to be one third of the absolute uncertainty. During MISR retrievals, in-flight measured radiometric uncertainty for each camera will be used directly for calculating the χ^2 test variables.

Here σ^2_{geom} (a dimensionless quantity) is the uncertainty in the camera-to-camera equivalent reflectance ratio, derived from the expansion of errors for a ratio of measurements $[\sigma^2(f(x, y))] = (df/dx)^2\sigma_x^2 + (df/dy)^2\sigma_y^2$ [e.g., *Bevington and Robinson*, 1992]):

$$\sigma^2_{\text{geom}}(l, k) = \frac{\sigma^2_{\text{cam}}(l, k)}{\rho^2_{\text{meas}}(l, \text{nadir})} + \frac{\sigma^2_{\text{cam}}(l, \text{nadir})\rho^2_{\text{meas}}(l, k)}{\rho^4_{\text{meas}}(l, \text{nadir})} \quad (3b)$$

where $\sigma_{\text{cam}}(l, k)$ is the contribution of (band l, camera k) to the camera-to-camera relative calibration reflectance uncertainty; σ_{cam} is nominally one third the corresponding value of σ_{abs} for the MISR instrument [*Diner et al.*, 1997]. Note that σ_{cam} includes the effects of systematic calibration errors for ratios of equivalent reflectance between cameras, as well as random error due to instrument noise, though the latter has been neglected in these simulations, based on the high signal-to-noise ratio demonstrated during MISR camera testing [*Bruegge et al.*, 1998].

Similarly, we define a spectral χ^2 as

$$\chi^2_{\text{spec}} = \frac{1}{N\langle w_k\rangle}\sum_{k=1}^{9}\frac{w_k\left[\dfrac{\rho_{\text{meas}}(\text{band } 4, k)}{\rho_{\text{meas}}(\text{band } 3, k)} - \dfrac{\rho_{\text{comp}}(\text{band } 4, k)}{\rho_{\text{comp}}(\text{band } 3, k)}\right]^2}{\sigma^2_{\text{spec}}(l, k)} \quad (4a)$$

with

$$\sigma^2_{\text{spec}}(l, k) = \frac{\sigma^2_{\text{band}}(l, k)}{\rho^2_{\text{meas}}(\text{band } 3, k)} + \frac{\sigma^2_{\text{band}}(\text{band } 3, k)\rho^2_{\text{meas}}(l, k)}{\rho^4_{\text{meas}}(\text{band } 3, k)} \quad (4b)$$

where $\sigma_{\text{band}}(l, k)$ is the contribution of (band l, camera k) to the band-to-band relative calibration reflectance uncertainty; σ_{band} is nominally one third the corresponding value of σ_{abs} for the MISR instrument.

We include a maximum deviation test variable that is the single largest term contributing to χ^2_{abs} (see equation (2)):

$$\chi^2_{\text{maxdev}} = \max_{l,k}\frac{[\rho_{\text{meas}}(l, k) - \rho_{\text{comp}}(l, k)]^2}{\sigma^2_{\text{abs}}(l, k)} \quad (5)$$

All the other test variables are averages of up to 18 measurements. The test variable χ^2_{maxdev} makes greatest use of any band-specific or scattering-angle-specific phenomenon, such as a rainbow or a spectral absorption feature, in discriminating between the measurements and comparison models.

2.2. Evaluating the χ^2 Test Variables

Since each χ^2 variable is normalized to the number of channels used, they are "reduced" χ^2 quantities, and a value less than or about unity implies that the comparison model is indistinguishable from the measurements. Values larger than about 1 imply that the comparison model is not likely to be consistent with the observations. In more detail, $\chi^2 < 1$ means that the average difference between the measured and comparison quantities is less than the associated measurement error. If the quantity in the numerator of a reduced χ^2 variable definition with 17 degrees of freedom is sampled from a population of random variables, an upper bound of 1 corresponds formally to an average confidence of about 50% that we are not rejecting a comparison model when in fact it should be accepted; for an upper bound of 2, that confidence increases to almost 99% [*Bevington and Robinson*, 1992]. (This is not strictly true for the "χ^2" variables defined here. They are actually the averages of correlated measurements from multiple bands and cameras, so a given upper bound is likely to be a less stringent constraint. Each term contributing to these variables may itself be distributed as χ^2.)

To illustrate the values of the test variables, we developed a color bar with three segments (Plate 1): a logarithmic segment for values between 10^{-5} and 1 depicted in shades of blue, a logarithmic segment for values between 5 and 10^4 depicted in shades of red, and a linear segment shown in light green, yellow, and orange shades for the intermediate values. Thus red shades in Plate 1 indicate situations where the model is clearly distinguishable from the measurement, whereas blue shades indicate that the model is indistinguishable from the measurement. Black is reserved for exact agreement between model and measurement, which can occur in this study because we are working with simulated observations. Note that the color table has been designed so that if Plate 1 is photocopied in black and white, first-order information about the ability to distinguish among models is preserved.

2.3. Organizing the Study of the Eight-Dimensional Space

There are four independent variables associated with aerosols from the "atmosphere" (τ_a, r_a, nr_a, and ni_a) and another four representing the same aerosol properties for the comparison models (τ_c, r_c, nr_c, and ni_c). We have defined four dependent variables to be used in comparing the measurements with the models (χ^2_{abs}, χ^2_{geom}, χ^2_{spec}, and χ^2_{maxdev}). This creates an eight-dimensional space, with four scalar elements at each point in the domain.

On the basis of climatological data we select natural ranges of aerosol optical depth, particle size distribution characteristic radius, and indices of refraction to study. Simulations are run for a grid of values in these four variables. We systematically explore the properties of this space by selecting a subset of

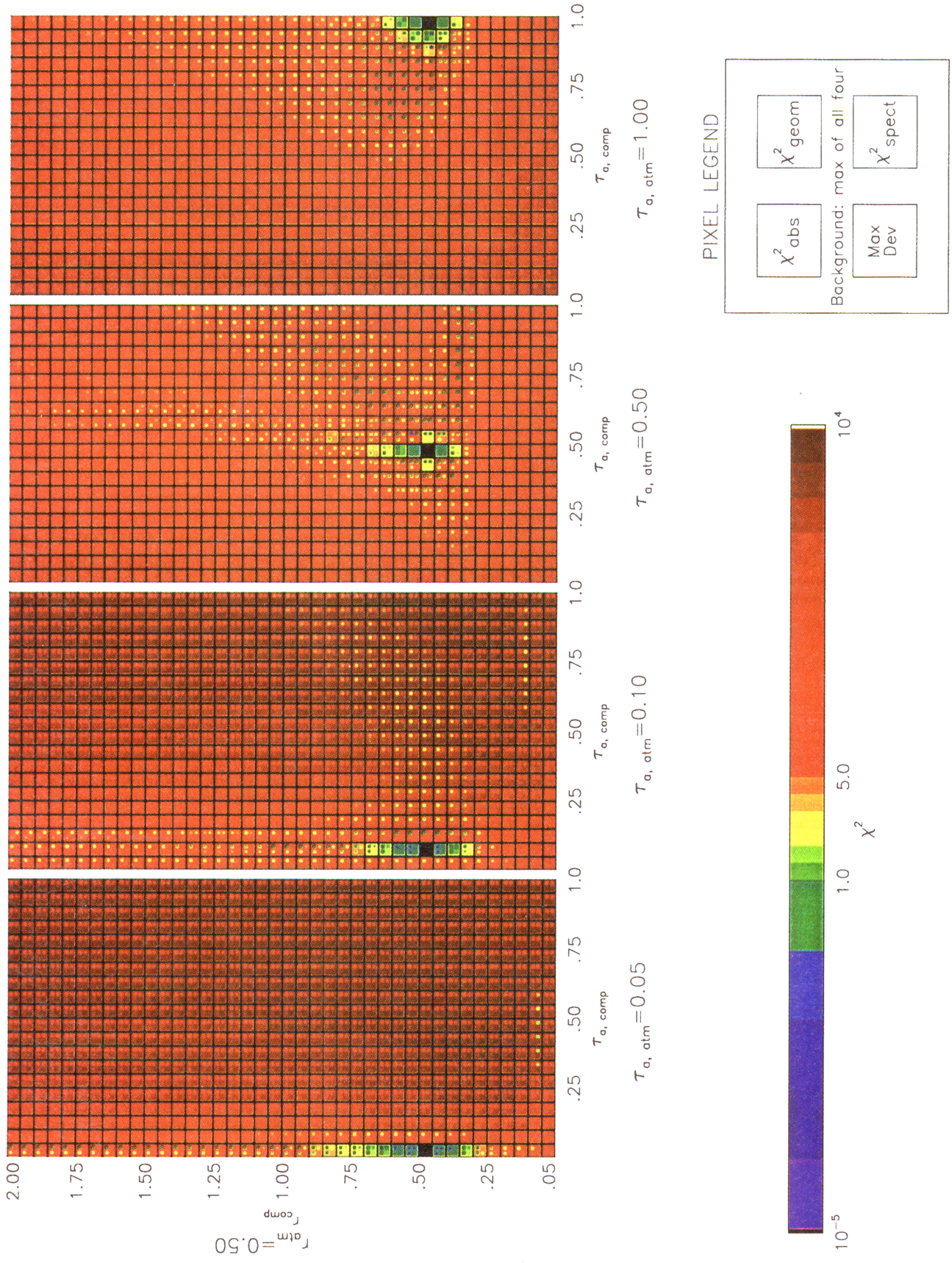
$\tau_{a,\,atm}$=0.05
$\tau_{a,\,atm}$=0.10
$\tau_{a,\,atm}$=0.50
$\tau_{a,\,atm}$=1.00
$\tau_{a,\,comp}$
τ_{atm}=0.50
τ_{comp}
.25
.50
.75
1.0
1.25
1.50
1.75
2.00
.05
PIXEL LEGEND
χ^2_{abs}
χ^2_{geom}
Background: max of all four
Max Dev
χ^2_{spect}
10^{-5}
1.0
5.0
10^4
χ^2

these values as the "atmosphere" cases and calculating all four test variables that compare each of the "atmosphere" cases with all the cases in the grid.

We built an interactive system that plots χ^2 values for any three independent variables. We can slice through this volume and display the color-bar values of any of the test variables, or for the maximum of the four test variables, in a two-dimensional plot. For each point in these plots we can call up the values of all the independent and dependent variables, as well as the calculated reflectance values for the associated atmosphere and comparison model. We also created a summary tool that searches numerically through the space, identifies the minimum and maximum values of any of the independent variables that meet user-specified criteria on the test variables, and displays the results as bar charts. These tools are illustrated in section 3. With them, we create general summaries of the retrieval sensitivity and can identify the specific equivalent reflectances that contribute to these results.

3. Sensitivity to Aerosol Optical Depth, Characteristic Radius, and Indices of Refraction

To capture in a sensitivity study the range of likely aerosol effects, we systematically explore the properties of three parameter spaces. They cover natural ranges of aerosol optical depth, particle size distribution characteristic radius, and indices of refraction for "nucleation," "accumulation," and "coarse" mode particles. Table 1 lists the ranges for all three parameter spaces. Simulations were run on a grid of linearly spaced values in all dimensions except the imaginary index of refraction, for which the grid spacing is logarithmic.

We concentrate on accumulation mode particles because they are expected to contribute most to total aerosol optical depth at visible wavelengths. Nucleation mode particles are much less efficient at extinguishing light, and coarse mode particles are usually rare. However, even for the accumulation mode size range, not all locations within the parameter space are likely to be filled by commonly occurring atmospheric aerosols. The properties of common aerosol types are summarized in Table 2. There are five basic compositions: sulfates, mineral dust, sea salt, biomass burning particles, and soot. Sizes range from tiny soot particles to coarse mineral dust and sea salt. With the exception of soot, particles have low imaginary index of refraction and high single scattering albedo in the red and near-infrared channels. This climatology helps constrain results in the operational MISR retrieval [*Martonchik et al.*, 1998]. We also use the climatology as a guide to interpreting the sensitivity calculations. (The present study deals with spherical particles. In the MISR retrievals and in our previous sensitivity study [*Kahn et al.*, 1997], mineral dust particles are treated as nonspherical.)

Table 1. Parameter Space of Aerosol Properties Used in This Study

	Minimum Value	Maximum Value	Number of Divisions
Aerosol optical depth at 0.55 μm	0.05	1.00	20
Real index of refraction	1.33	1.55	12
Imaginary index of refraction	0.0	0.50	20
Nucleation mode characteristic radius	0.005	0.2	40
Accumulation mode characteristic radius	0.05	2.00	40
Coarse mode characteristic radius	0.50	4.50	41

*For the nucleation mode, there are 20 increments of optical depth, ranging from 0.025 to 0.50.

3.1. Constraints on Aerosol Optical Depth

We begin with the question: Given MISR data over a cloud-free, dark ocean surface, how well can we constrain the optical depth (τ_a) of atmospheric aerosols?

Plate 1 is an example of a comparison matrix, taken from within the accumulation mode parameter space. In Plate 1, the atmospheric particles have fixed microphysical properties typical of sulfate particles in the troposphere [e.g., *Shettle and Fenn*, 1979]: dry values of $nr_a = 1.53$, $ni_a = 0.0$, and log-normal size distribution with $r_a = 0.5$ μm and width of 1.86. The particles are hydrated to equilibrium at 70% relative humidity, using the model of *Hanel* [1976].

There are four panels in Plate 1. Each contains all the test results for one choice of atmospheric optical depth, so within a panel, all the modeled properties of the atmospheric aerosols are fixed. The four panels correspond to atmospheric aerosol optical depths at 0.55 μm wavelength of 0.05, 0.1, 0.5, and 1.0, respectively.

The optical depths of the comparison models at 0.55 μm vary systematically from 0.05 to 1.0 in increments of 0.05 across the bottom of each panel in Plate 1; the dry radii of the comparison models vary from 0.05 to 2.0 μm in increments of 0.05 along the vertical axis. Refractive indices for the comparison model are the same as those for the atmosphere in the slice shown here.

Each box within the panel is divided into five fields, four showing the colors corresponding to each of the χ^2 test variables, and the background, which is colored with the largest (most red) χ^2 value among the four tests. So the box for each comparison model tells whether that model can be distinguished from the atmosphere with MISR data and which test(s) provides the most constraining information.

In Plate 1 the blue areas, which indicate comparison models indistinguishable from the atmosphere with MISR data, are small and vertically oriented: there are acceptable comparison models with a broad range of r_c but a narrow range of τ_c on this scale. Close examination of the surrounding boxes shows that χ^2_{maxdev} and χ^2_{abs} are responsible for constraining τ_c so tightly. Both tests rely on the absolute brightness. This is ex-

Plate 1. (opposite) Example of a comparison matrix. This shows the results of tests between an atmosphere containing tropospheric sulfate-like particles and comparison models with ranges of optical depth and characteristic radius. For this example, all particles have initial (dry) indices of refraction set to nr = 1.53, ni = 0.0 and are hydrated to equilibrium with 70% relative humidity following *Hanel* [1976]. The four panels correspond to atmospheric aerosol optical depths of 0.05, 0.1, 0.5, and 1.0 at 0.55 μm wavelength. In blue and black areas the largest value for any test variable is <1, indicating that the comparison models that are indistinguishable from the simulated MISR data. Red areas indicate comparison models that are not consistent with the MISR observations. The calculations presented here and elsewhere in this paper are for mid-latitude cases: the cosine of the solar zenith angle (μ_0) is 0.6, and the angle between the azimuth of the Sun and the instrument viewing plane ($\Delta\phi$) is 26.0°.

Table 2. MISR Climatology of Pure Particle Types

Aerosol Type	r_1, μm	r_2, μm	r_c, μm	σ	α	nr	ni (Band)	ω_0 (0.67 μm)	Shape	RH, %	Vary With RH?
Sulfate 1 (accumulation)	0.007	0.7	0.2	1.86	n/a	1.53	0.0 (all)	1.0	spheres	0	yes
Sulfate 2* (accumulation)	0.05	2.0	0.45	1.30	n/a	1.43	0.0 (all)	1.0	spheres	ambient	no
Mineral dust† (accumulation)	0.05	2.0	0.47	2.60	n/a	1.53	0.0085(1) 0.0055(2) 0.0045(3) 0.0012(4)	0.91	prolate/oblate spheroids	0	no
Mineral dust† (coarse)	0.5	15.0	1.90	2.60	n/a	1.53	0.0085(1) 0.0055(2) 0.0045(3) 0.0012(4)	0.70	prolate/oblate spheroids	0	no
Sea salt (accumulation)	0.05	1.0	0.35	2.51	n/a	1.50	0.0 (all)	1.0	spheres	0	yes
Sea salt (coarse)	1.0	20.0	3.30	2.03	n/a	1.50	0.0 (all)	1.0	spheres	0	yes
Soot	0.001	0.5	0.012	2.00	n/a	1.75	0.455(1) 0.440 (2) 0.435 (3) 0.430 (4)	0.17	spheres	0	no
Biomass burning‡	0.007	2.0	0.13	1.80	n/a	1.43	0.0035 (all)	0.98	spheres	97	no
Near-surface fog§	0.5	50.0	n/a	n/a	2.5	1.33	0.0 (all)	1.0	spheres	100	no
Thin cirrus¶	10.0	500.	n/a	n/a	n/a	1.31	0.0 (all)	1.0	fractal	100	no

Here r_1 and r_2 are the lower and upper radius limits for the particle size distribution. Particle types having r_c and σ specified are distributed lognormally, with characteristic radius r_c and width σ; those having α specified are power law distributions with exponent α (n/a, not applicable); ω_0 is the single scattering albedo, given at the effective wavelength of the MISR red channel. RH is the relative humidity for which the particle size distribution and indices of refraction are listed. The last column indicates that the properties of sulfate 1 and sea salt particles are assumed to vary with relative humidity, using the hydration model of *Hanel* [1976]. The aerosol physical data are abstracted from *Shettle and Fenn* [1979], *d'Almeida et al.* [1991], *World Climate Programme WCP-112* [1984], and other sources, except as indicated. Optical data for spherical particles are calculated using Mie theory.

*Stratospheric aerosol model based on work by *Wang et al.* [1989].
†Nonspherical mineral dust models based on work by *Mishchenko et al.* [1997].
‡Biomass burning particle model based on work by *Remer et al.* [1998].
§Near-surface fog model based on work by *Prupacker and Klett* [1978].
¶Fractal thin cirrus model based on work by *Mishchenko et al.* [1996].

pected, since the absolute scene brightness increases with optical depth for nonblack particles over a black surface.

We have studied sensitivity to optical depth over the entire parameter spaces given in Table 1. The results for accumulation and coarse mode particles are summarized in Figures 2a and 2b, respectively. These bar charts show the sensitivity, as indicated by the range of acceptable comparison model optical depth, along the vertical axis for all comparison models in the accumulation mode parameter space that give acceptable matches to an atmosphere with fixed particle properties. For Figures 2a and 2b an acceptable comparison model is one for which all four χ^2 test variables fall between 0 and 2.

Each group of four bars corresponds to four choices of atmosphere particle optical depth (0.05, 0.1, 0.5, and 1.0 in MISR band 2) for fixed atmosphere particle radius. The groups are spread along the horizontal axis to indicate different choices of atmosphere particle radius. Each panel of Figure 2 represents a fixed value of atmosphere particle imaginary index of refraction. The real index of refraction for atmosphere particles is fixed at 1.47 for all these charts, but within its natural range of values this quantity has very little effect on these results.

So for each bar, all the atmospheric particle properties have been fixed. The comparison model properties, r_c, nr_c, and ni_c, have been varied over the entire parameter space given in Table 1. The comparison models having the largest and smallest values of τ_c that meet the test criteria, regardless of the values of the other three comparison model parameters, determine the upper and lower limits of the bar.

Sensitivity to optical depth is as low as 0.05 and remains within 20% regardless of the physical properties of the particles, as long as ni_a is 0.0. This covers all natural cases involving sulfate and sea salt particles (Table 2). The lower limit of 0.05 is set by the assumed camera calibration uncertainty, which reaches a limiting value for low reflectance levels (Figure 1). Calibration uncertainty affects the sensitivity through "σ" in the χ^2 test variable definitions. The choice of grid spacing for this study was made in consideration of this limit. During MISR operations, in-flight measured radiometric uncertainty for each camera will be used directly for calculating the χ^2 test variables in the retrievals [*Bruegge et al.*, 1998].

According to Figure 2, as ni_a increases, sensitivity to aerosol optical depth degrades and becomes more dependent on atmospheric aerosol optical depth, particle size, and imaginary refractive index. Sensitivity to τ_a also decreases as optical depth increases, particularly from 0.05 to 0.5. Part of the degradation comes from the increased contribution of multiple scattering to the signal as scene brightness increases. For example, when r = 0.5 μm, nr = 1.47, and ni = 0.13, the multiple scattering contribution to the steepest forward looking MISR camera increases from about 20% of the signal to nearly half as τ increases from 0.1 to 0.5. As τ_a increases further, the sensitivity to optical depth increases again in some cases. Here the multiple scattering contribution is not growing as rapidly, whereas the total aerosol signal relative to background Rayleigh scattering continues to increase. (The upper boundary for each chart corresponds to the maximum value in the parameter space, so the high-side uncertainty for these cases is not shown. Owing to the number of computations needed for this study, it was impractical to expand the param-

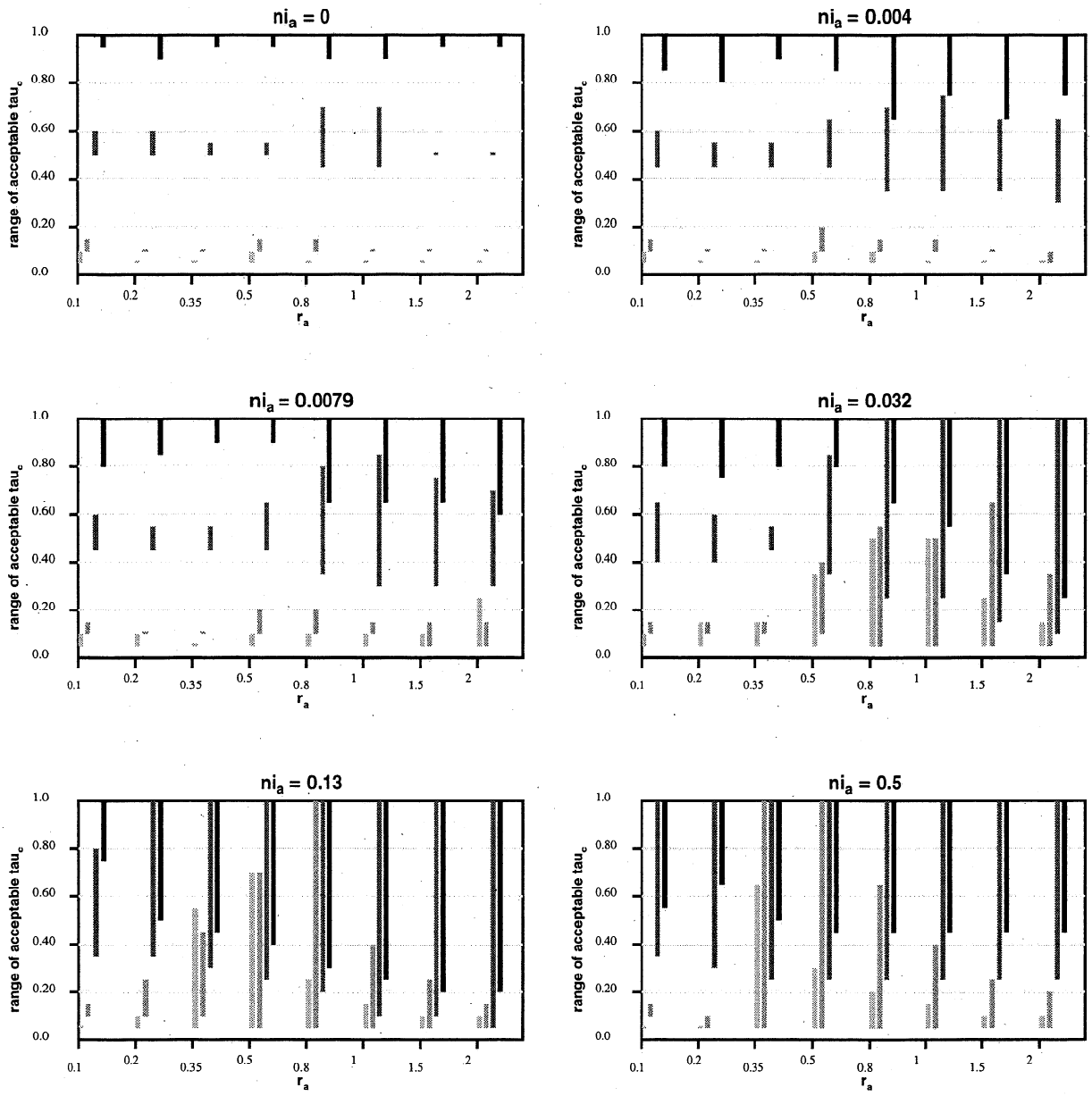

Figure 2a. Bar chart showing the ranges of aerosol optical depth values (τ_c) for comparison models that give acceptable matches to an atmosphere with accumulation mode particles having real index of refraction $nr_a = 1.47$, imaginary index of refraction ni_a ranging from 0.0 to 0.50. For an acceptable match, all four χ^2 test variables must fall between 0 and 2. Bars are produced for eight choices of atmospheric particle characteristic radius (r_a) between 0.1 and 2, arrayed along the horizontal axes. For each r_a a group of four bars is produced, corresponding to four choices of atmospheric optical depth (τ_a). As shading increases, the bars represent values of τ_a increasing from 0.05 to 0.1, 0.5, and 1.0.

cter space beyond the limits shown. The reflectance tends to asymptote as optical depth increases beyond 1. For large optical depth the high-side uncertainty is comparable to the low-side uncertainty but grows larger than the low-side uncertainty as particle size and imaginary index of refraction increase. Cases away from the limiting values provide a sense for the sizes of these trends.)

We now examine in detail the sensitivity of the multiangle retrieval to particles that have nonzero ni. When ni = 0.0, most of the information about optical depth comes from systematic increases in brightness as τ increases. As Figure 3 shows, when ni > 0.0, the single scattering phase functions in the backscattering directions decrease with increasing radius. For a given set of measured radiances, we find agreement based on the χ^2 criteria for several comparison models, some with smaller radius and lower optical depth, others with larger radius and higher optical depth. This creates the higher uncertainty in τ_c found in Figure 2.

For the MISR retrieval we are most interested in climatologically likely aerosol types. Among these, biomass burning particles, mineral dust, and soot have nonzero ni, and only soot in climatologically high concentrations is likely to affect the quality of the MISR global aerosol products.

In the red and near-infrared channels, ni for biomass burn-

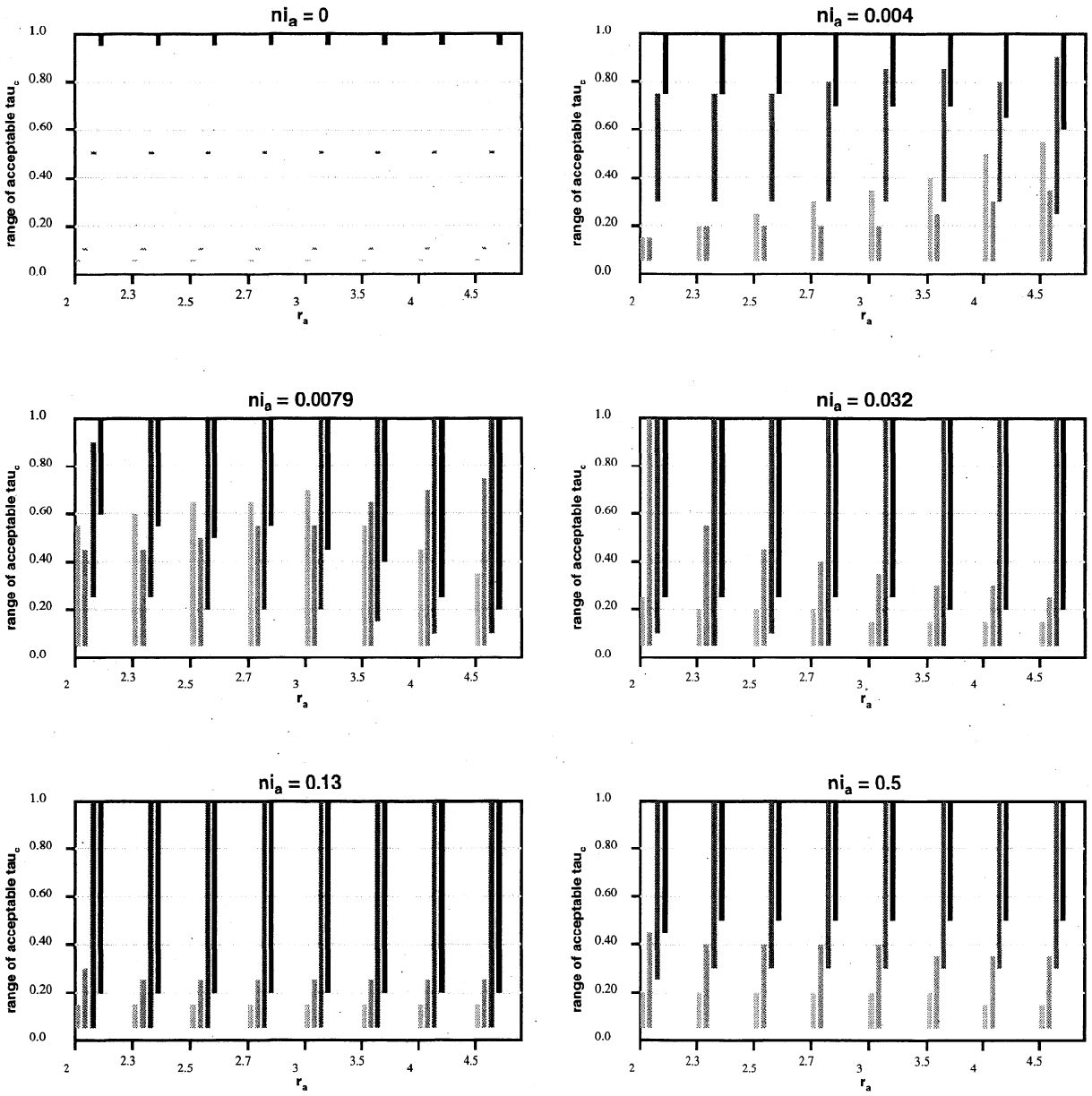

Figure 2b. Same as Figure 2a but for part of the coarse mode particle parameter space.

ing particles in Table 2 is around 0.004. For all accumulation mode particles and for optical depths less than 0.5 the range of optical depth for acceptable comparison models falls within 20% of the atmospheric value. This covers the expected natural range of conditions except near source regions, which are on land but may be close to a coast. If column optical depths of these particles reach 0.5 or if coarse-sized biomass burning particles form, the sensitivity of MISR to optical depth will be diminished. (Note that the differences between the bars for $r_a = 2$ μm in corresponding charts of Figures 2a and 2b arise because the ranges of comparison model particle sizes for the two cases are different (Table 1).)

For mineral dust, ni in Table 2 for the red channel is also about 0.004, a value representative of the optically important dust component in many global studies [e.g., *Tegen and Lacis*, 1996]. However, a great variety of mineral dust particle types are known to occur in nature [*Sokolik and Toon*, 1996]. With increasing ni$_a$ or r_a, sensitivity to optical depth degrades. In the climatologically unlikely situation that optical depths of a few tenths or more of coarse mode dust are present over ocean, or ni$_a$ exceeds 0.008, the retrieved optical depth will be uncertain to 25% or more. If no other information is available, MISR results will depend upon the assumptions we make about mineral dust properties, particularly regarding the imaginary index of refraction. However, MISR data can distinguish spherical from natural mixes of nonspherical mineral-dust-like particles. This is an advantage over previous remote sensing aerosol retrievals and is expected both to help identify mineral dust and to bring the optical depth sensitivity within 20% or 0.05, whichever is larger, for many natural situations [*Kahn et al.*, 1997].

The poorest sensitivity to optical depth occurs when dark particles (those having large ni) are found over the dark ocean surface. Soot particles fall into this category, but they are smaller than the other particle types in Table 2 and lie below the size ranges covered in Figure 2. Figure 4 explores this case,

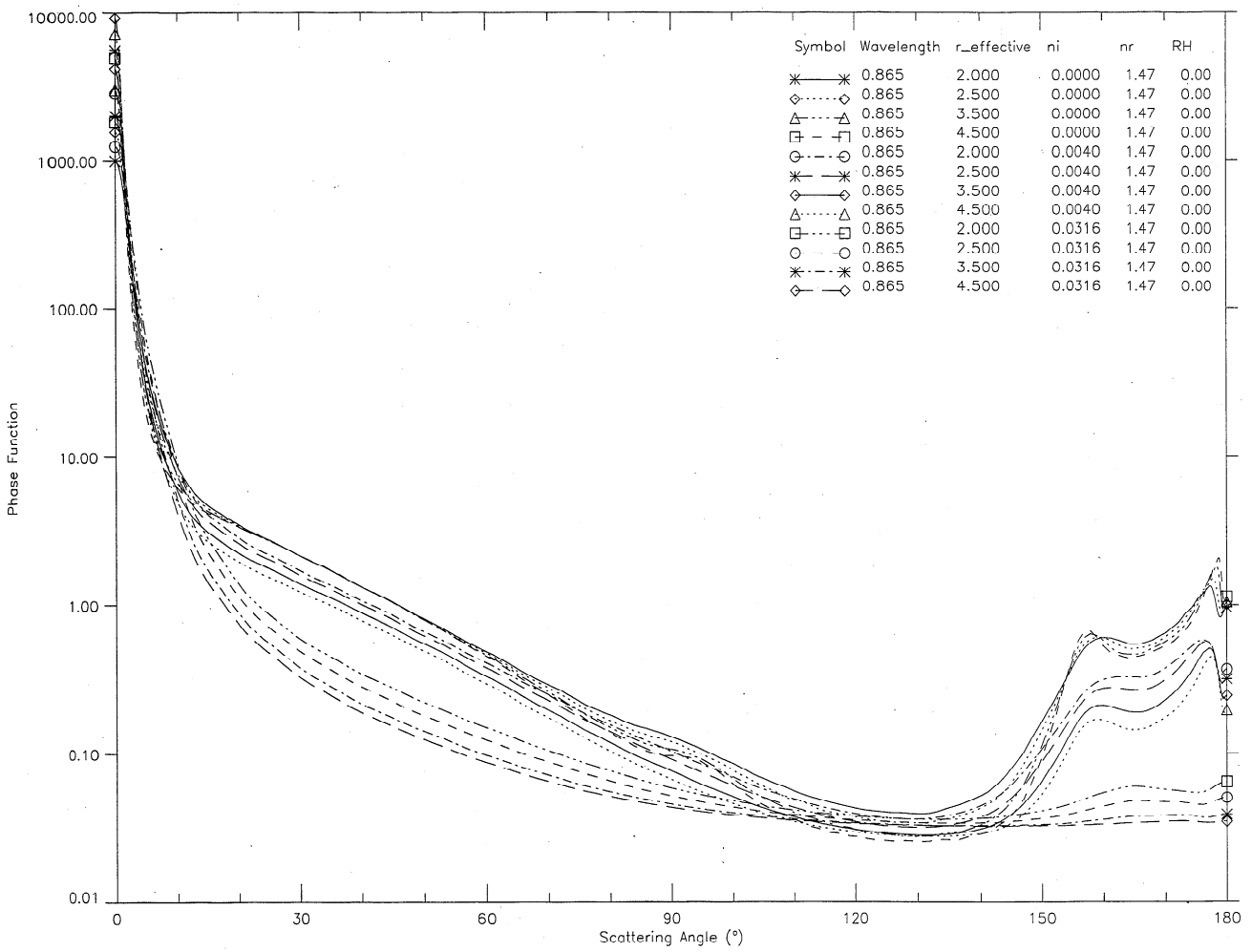

Figure 3. Particle scattering phase functions at the effective wavelength of the MISR near-infrared band for single-sized spherical particles in the coarse mode range, between 2.0 and 4.5 μm radius, and nr = 1.47. Three groups of phase functions are plotted, one with ni = 0.0, one with ni = 0.004, and one with ni = 0.032. These three groups correspond to the uppermost, middle, and lowest four lines, respectively, when viewed at scattering angles between 150° and 180°, the region where much of the MISR optical depth discrimination is made.

giving bar charts for part of the nucleation mode parameter space. It shows that even for tiny particles, multiangle data are not sensitive to the optical depth of very dark particles over a dark surface. This is an inherent limitation of the technique. On the spatial scale of 17.6 km that applies to the MISR aerosol product we expect that optical depths for pure soot will rarely exceed a few tenths over ocean. In addition, soot is most likely to appear mixed with other particle types having much lower ni. Our sensitivity to optical depth for such mixtures may be higher and is the subject of continuing work.

On the basis of the results of this section, we expect the MISR aerosol optical depth retrieval sensitivity over ocean to fall within 0.05 or 20%, whichever is larger, for climatologically likely aerosol situations. With the actual MISR data, we may be able to decrease the limiting χ^2 test value below 2, which would lead to a tighter optical depth constraint. However, the measurements are insensitive to soot or to dark mineral particles with optical depth for τ_a greater than about 0.1. We plan to use in situ measurements whenever possible to improve our assumptions about particle properties.

3.2. Constraints on Particle Characteristic Radius

We now ask the question: Given MISR data over a cloud-free, dark ocean surface, how well can we constrain the characteristic radius (r_a) of a monomodal distribution of atmospheric aerosols?

Figure 5a is a bar chart showing the ranges of r_c for all the comparison models in the accumulation mode parameter space that give acceptable matches to an atmosphere with fixed particle properties. Figure 5b is a similar set of charts for coarse mode sizes. In these charts the real index of refraction for the atmosphere particles (nr_a) varies from column to column, and the imaginary index of refraction (ni_a) varies from row to row. Comparison model properties, τ_c, nr_c, and ni_c, are free to vary over the entire parameter space given in Table 1. An acceptable match is a case for which all four χ^2 test variables fall between 0 and 2. Bars are produced for eight choices of atmospheric particle radius (r_a) in each mode. For each r_a, bars are produced for four choices of atmospheric optical depth τ_a (0.05, 0.1, 0.5 and 1.0) in MISR band 2.

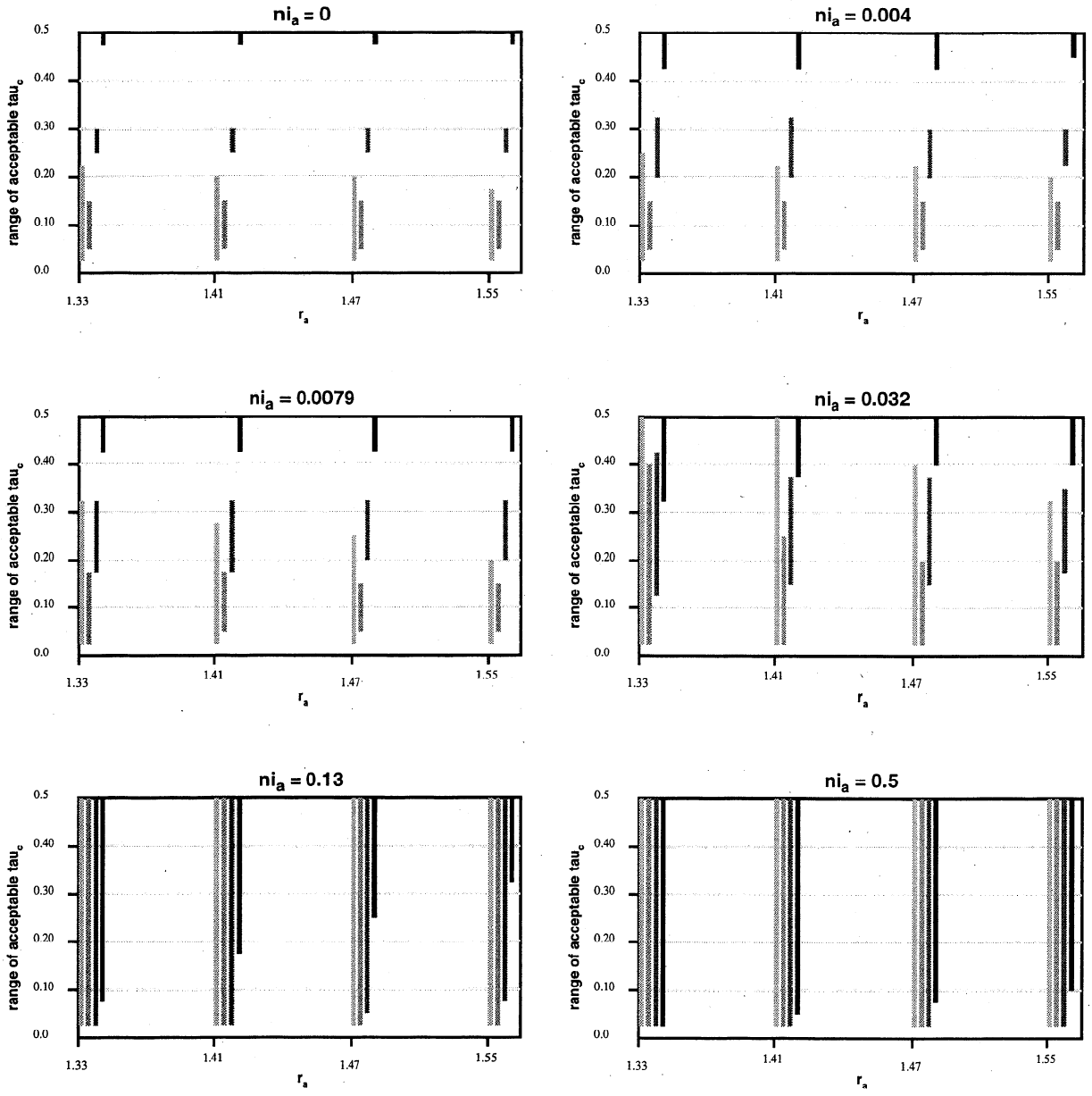

Figure 4. Bar chart showing the ranges of aerosol optical depth values (τ_c) for comparison models that give acceptable matches to atmosphere particles covering part of the nucleation mode parameter space that includes expected soot particle sizes and indices of refraction. Atmosphere particle characteristic radius is fixed at 0.01 μm. The imaginary index of refraction ni_a ranges from 0.0 to 0.50. For an acceptable match, all four χ^2 test variables must fall between 0 and 2. Bars are produced for four choices of real index of refraction (nr_a) between 1.33 and 1.55, arrayed along the horizontal axes. For each nr_a, a group of four bars is produced, corresponding to four choices of atmospheric optical depth (τ_a). As shading increases, the bars represent values of τ_a increasing from 0.025 to 0.05, 0.25, and 0.5.

At each r_a, the range of acceptable r_c generally decreases as τ_a increases. This means we have better constrained aerosol characteristic radius retrievals with increasing τ_a. We expect such behavior: by increasing the amount of aerosol, the contribution of aerosols to the measured radiance is increased, relative to the contribution from Rayleigh scattering gas. Some exceptions occur when increased instrument radiometric uncertainty, caused by the greater scene brightness (Figure 1), is enough to offset the increased aerosol signal.

Especially when τ_a is greater than 0.05, the constraint on r_c is tight for accumulation mode atmospheric particle distributions with characteristic radius smaller than about 0.8 μm. For larger particles, r_c is poorly constrained by simulated MISR data over ocean. This behavior is traced to the particle scattering phase function, which goes through a transition from "small" (Rayleigh) to "large" (geometric) regimes as particle size increases. At midlatitudes and high latitudes, the instrument samples scattering angles ranging from about 60° to 160° (Figure 6). Over this range of scattering angles the particle single scattering phase functions change rapidly as r_a increases, until an upper limit is reached (Figure 7). For ni = 0.0, the transition occurs around r_a = 0.8 μm; for nonzero ni within

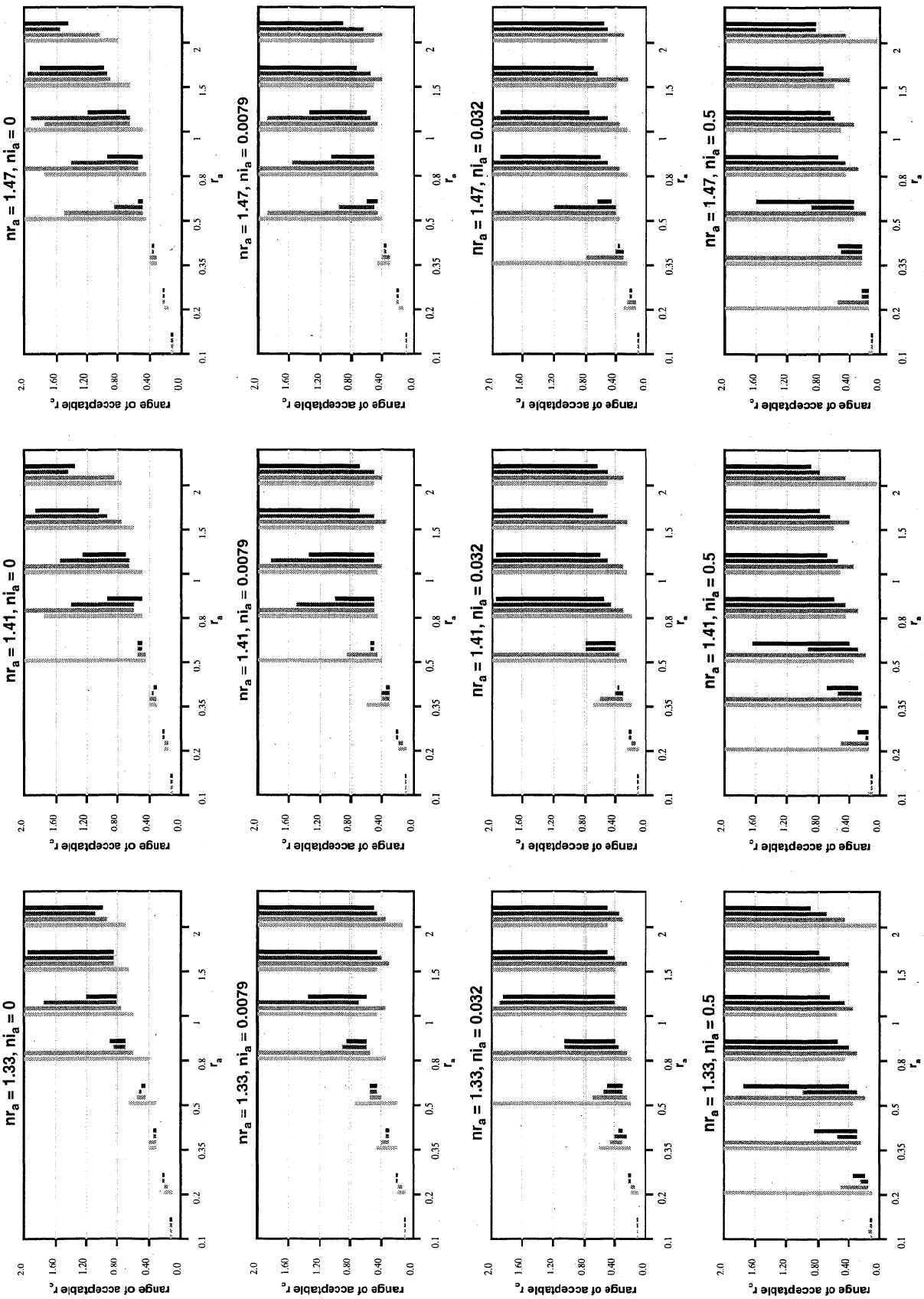

Figure 5a. Bar chart showing the ranges of particle radius (r_c) for comparison models that give acceptable matches to an atmosphere with accumulation mode particles having selected values of real and imaginary indices of refraction. For an acceptable match, all four χ^2 test variables must fall between 0 and 2. Bars are produced for eight choices of atmospheric particle radius (r_a). For each r_a, a group of four bars is produced, corresponding to four choices of atmospheric optical depth τ_a. As shading increases, the bars represent values of τ_a increasing from 0.05 to 0.1, 0.5, and 1.0.

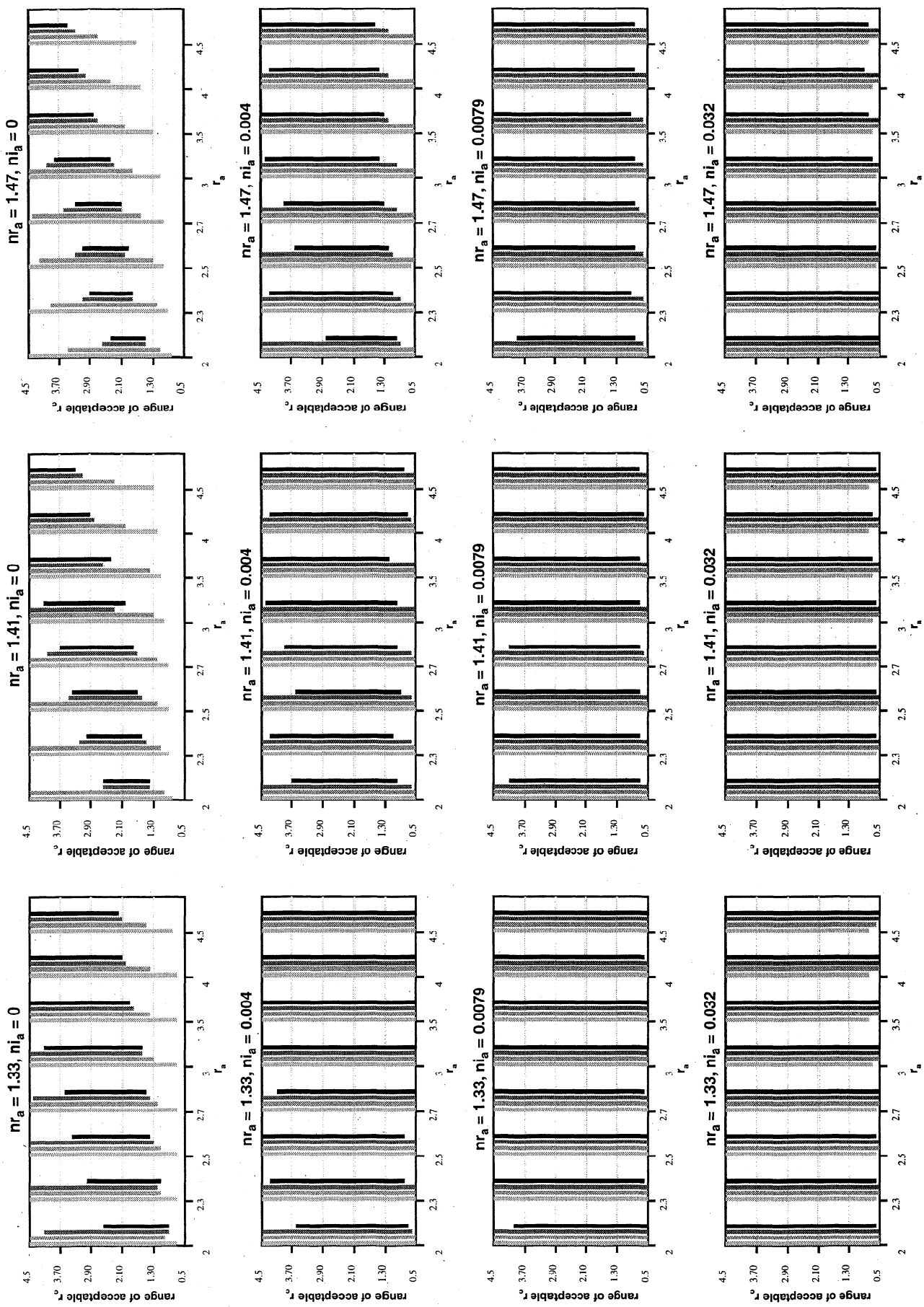

Figure 5b. Same as Figure 5a but for part of the coarse mode particle parameter space.

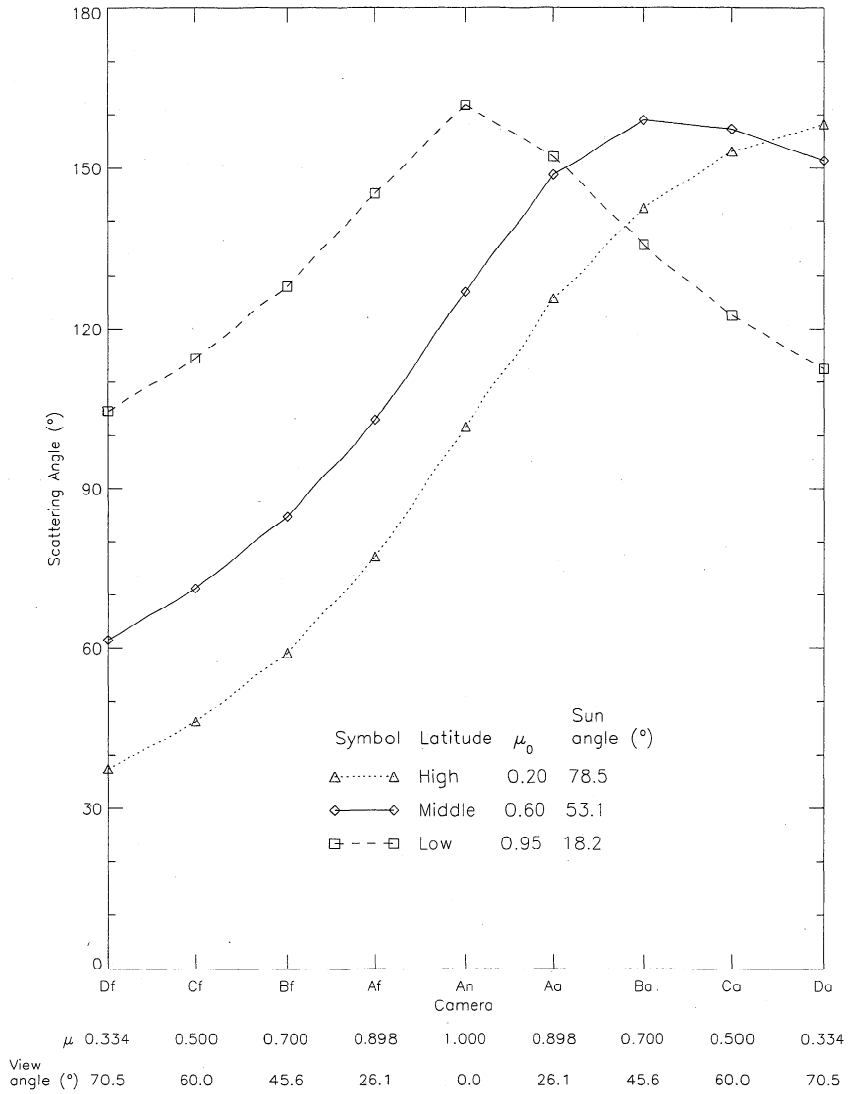

Figure 6. Typical ranges of scattering angles covered by the nine MISR cameras in the nominal EOS-AM orbit at high, middle, and low latitudes.

the natural range the transition occurs at r_a approaching 0.5 μm.

On the basis of Figure 5, MISR should be able to distinguish three to four groups of characteristic radius across the natural range of particle size, even if little is known a priori about composition, as long as the optical depth is greater than about 0.05. Most of this sensitivity occurs for particles with r_c between 0.1 and about 1 μm. The sensitivity to characteristic radius increases for higher optical depth and is greatest for particles with low imaginary index of refraction.

3.3. Constraints on Aerosol Composition

Figures 8 and 9 illustrate the sensitivity of MISR to real and imaginary indices of refraction, respectively. These parameters describe the composition of aerosols in our retrievals. As with particle size, sensitivity increases with atmospheric optical depth and decreases for darker particles within the parameter space.

For ni = 0, our ability to constrain nr depends on τ_a and r_a. MISR sensitivity to index of refraction increases greatly for increasing τ_a. Sensitivity to nr is diminished for the smallest particles (r_a = 0.1), which fall in the Rayleigh scattering regime (Figure 7). Our ability to discriminate nr is best for "medium" (accumulation mode) aerosols, and decreases for both small and large particles.

Overall, one to two groups of nr values can be distinguished over the natural range spanning nr = 1.33 to nr = 1.55, when τ_a is about 0.1. The number of groups increases to two to three nr values when τ_a is about 0.5, as long as the particles are not strongly absorbing. However, the data become insensitive to the real part of the index of refraction for darker particles (imaginary index larger than about 0.01).

Sensitivity to the imaginary part of the index of refraction itself follows a similar pattern, though the simulations suggest that when τ_a is 0.5 or greater, three to four groups of values between ni = 0.0 and about 0.5 can be distinguished. For optical depths of a few tenths, more typical of global ocean conditions, one or two groups of ni can be separated in the data.

3.4. Additional Considerations

The MISR instrument samples a broad range of scattering angles, between about 60° and 160°, in midlatitudes and high

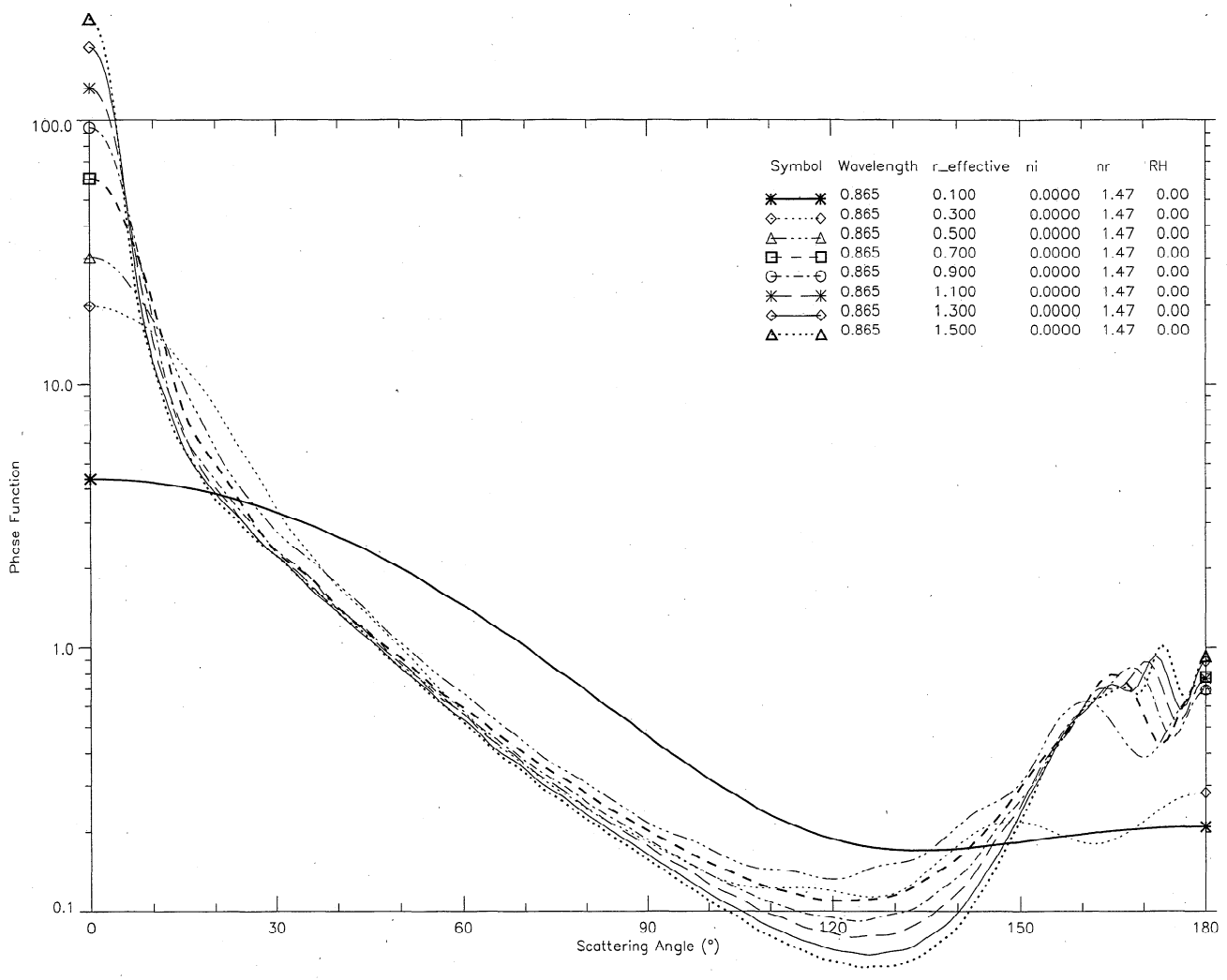

Figure 7. Particle scattering phase functions at the effective wavelength of the MISR near-infrared band for single-sized spherical particles with nr = 1.47, ni = 0.0, and radii ranging from 0.1 to 1.50 μm. This range covers the transition from small particle (Rayleigh) scattering to large particle scattering.

latitudes (Figure 6). The analysis presented in this paper is for midlatitude geometry. However, at low latitudes the range of scattering angles is diminished. This reduces the retrieval sensitivity to particle properties. Sensitivity to aerosol properties is also reduced if clouds are present or if the surface is not black in red and near-infrared wavelengths due to whitecaps, Sun glint, or plankton in the water. For MISR retrievals, we eliminate data from any cameras contaminated by Sun glint, since modeling Sun glint radiance would introduce large uncertainties. We model whitecaps, which involves making assumptions about how they behave [e.g., *Martonchik et al.*, 1998]. All these phenomena are expected at some times and places in the MISR data. The goal of the present study is to explore the sensitivity of MISR to particle properties using simulated data, under the best observing conditions we anticipate. By analyzing actual MISR data, obtained under real observing conditions, we will assess how actual retrieval sensitivities compare to the idealized cases considered here.

4. Conclusions

The enhanced ability of multiangle imaging to constrain aerosol properties, as compared to single-angle methods currently in operational use, comes from the known, varying geometric path through the atmosphere and the range of scattering angles observed. Over ocean, MISR retrieval results are based on assumed surface reflectances and assumptions that the atmosphere is cloud-free and the particles are horizontally homogeneous over the sampling region, which is 17.6 km at the surface, increasing to about 100 km at the tropopause for the nominal instrument viewing geometry.

On the basis of our study of simulated data for pure particles, MISR retrievals over dark ocean will provide information about atmospheric aerosol optical depth, and some constraints on aerosol microphysical properties:

4.1. Aerosol Optical Depth

We can retrieve column optical depth from measurements over calm ocean for all but the darkest particles, with typical size distributions and compositions, to an uncertainty of at most 0.05 or 20%, whichever is larger, even if the particle properties are poorly known. As particle imaginary index of refraction increases, sensitivity to optical depth degrades and becomes dependent on particle size and optical depth. For optical depths <0.5 and for particle sizes and indices of refrac-

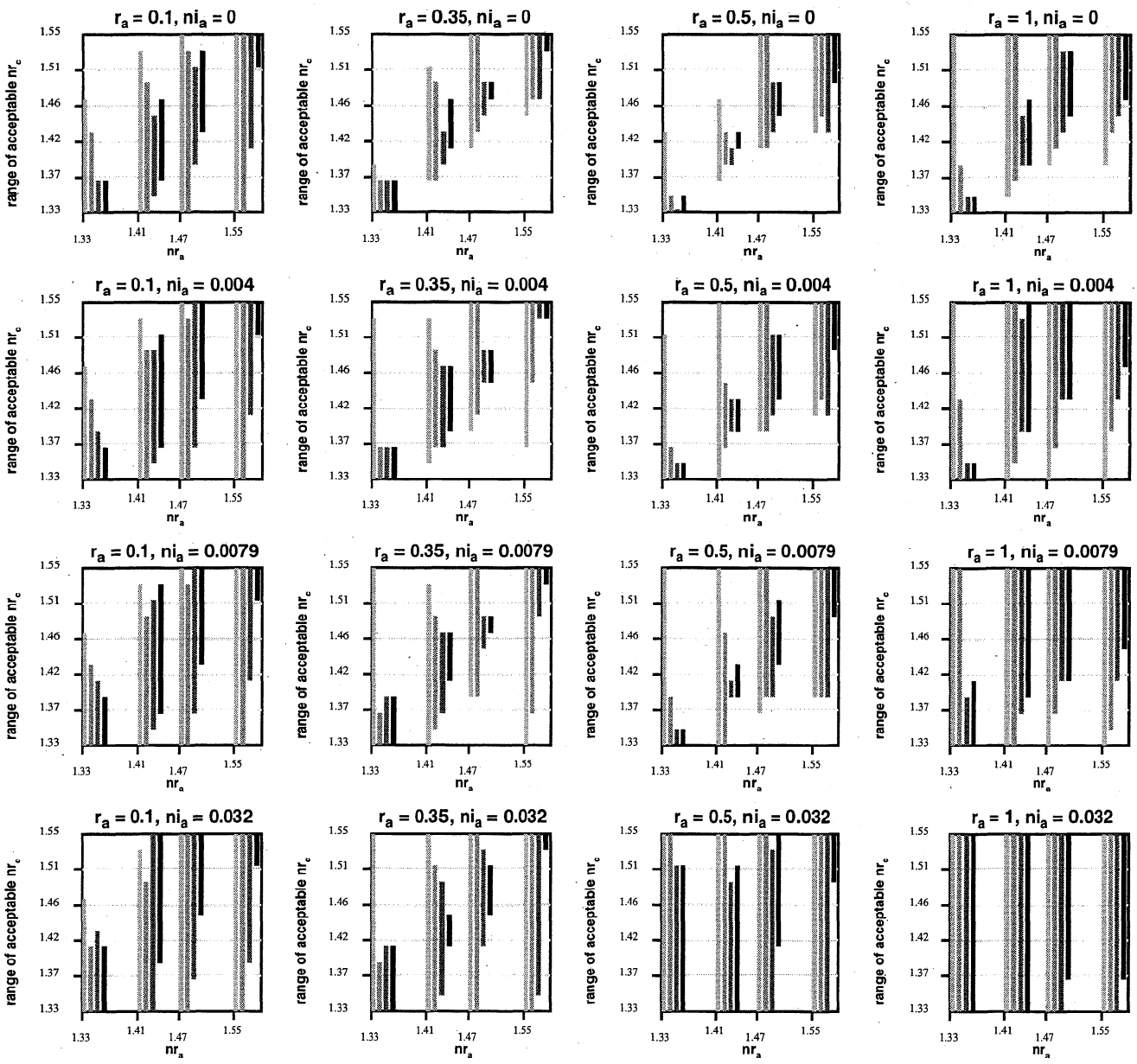

Figure 8a. Bar chart showing the ranges of particle real index of refraction (nr_c) for comparison models that give acceptable matches to an atmosphere with accumulation mode particles having selected values of characteristic radius and imaginary index of refraction. For an acceptable match, all four χ^2 test variables must fall between 0 and 2. Bars are produced for four choices of atmospheric particle real index of refraction (nr_a). For each nr_a a group of four bars is produced, corresponding to four choices of atmospheric optical depth (τ_a). As shading increases, the bars represent values of τ_a increasing from 0.05 to 0.1, 0.5, and 1.0.

tion expected for all common particle types except soot (Table 2), optical depth sensitivity is still better than 20%. The measurements are less sensitive to optical depth for common mineral dust and biomass burning particles with τ_a of 0.5 or greater and are insensitive to τ_a for soot.

4.2. Aerosol Size Distribution

We expect MISR to be able to distinguish three to four groups of characteristic radius across the natural range (small, medium, and large) over midlatitude and high-latitude ocean, even if little is known a priori about composition, as long as the aerosol optical depth is greater than about 0.05. Most of this sensitivity occurs for particles with r_c between 0.1 and about 1 μm, which covers the range of particle sizes where the scattering phase functions change from Rayleigh scattering behavior to curves with well-developed forward and back scattering peaks. The sensitivity to characteristic radius increases for higher optical depth, since there is more aerosol signal in these cases, and is greatest for less absorbing (low imaginary index of refraction) particles.

4.3. Aerosol Composition

MISR sensitivity to index of refraction increases strongly with increasing optical depth and decreases with increasing ni. We can distinguish about two or three groups of real index of refraction values between 1.33 and 1.55, as long as the optical

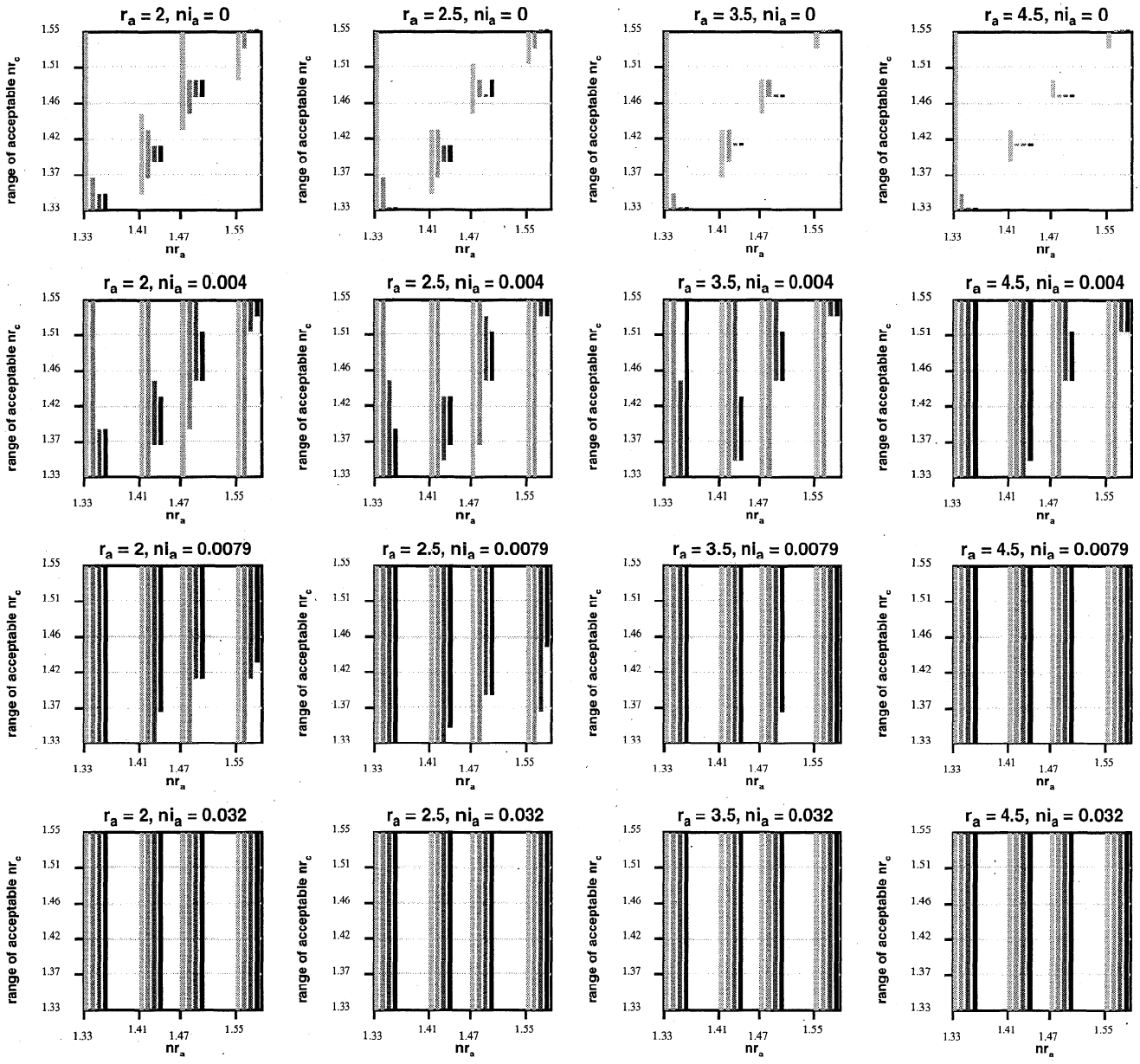

Figure 8b. Same as Figure 8a but for part of the coarse mode particle parameter space.

depth is 0.5 or larger and the particles are not strongly absorbing. Only one to two groups of nr values can be distinguished over the natural range when τ_a is about 0.1 or less. In addition, the data discriminate nr best for "medium" sized particles and are insensitive to the real part of the index of refraction for dark particles. Sensitivity to the imaginary part of the index of refraction follows a similar pattern, though the simulations suggest that three to four groups of values for ni between 0.0 and about 0.5 can be distinguished when τ_a is 0.5 or greater.

The actual sensitivity of MISR retrievals to particle properties over ocean will depend in part on the in-flight instrument calibration uncertainty, which sets the values of the σ, and governs our choice of the upper limit on χ^2 for accepting a comparison model as indistinguishable from the measurements. For this paper we used prelaunch instrument specifications for calibration and noise levels. After launch we will use the tools and the approach developed here to assess the in-flight sensitivity of MISR.

Our results suggest MISR will be able to distinguish small, medium, and large particle sizes, "dirty" or "clean" compositions, and "spherical" and "nonspherical" shapes, over the range of aerosol properties commonly found in nature. This should allow us to distinguish among the climatologically common particle types (Table 2) if each type occurs unmixed in the vertical column. We will use this improvement over simply assuming all the physical properties of particles, as is currently done for satellite aerosol monitoring, to identify air masses containing different aerosol types, as well as to provide more accurate retrievals of aerosol optical depth.

The strength of satellite retrievals is in their spatial and temporal coverage, which complements detailed composition and size distribution information that may be obtained locally from in situ measurements. We plan to rely on ground-based and in situ instrument data to derive detailed aerosol compositions and size distributions in air masses whenever possible.

This approach is similar to the way satellite-derived sea

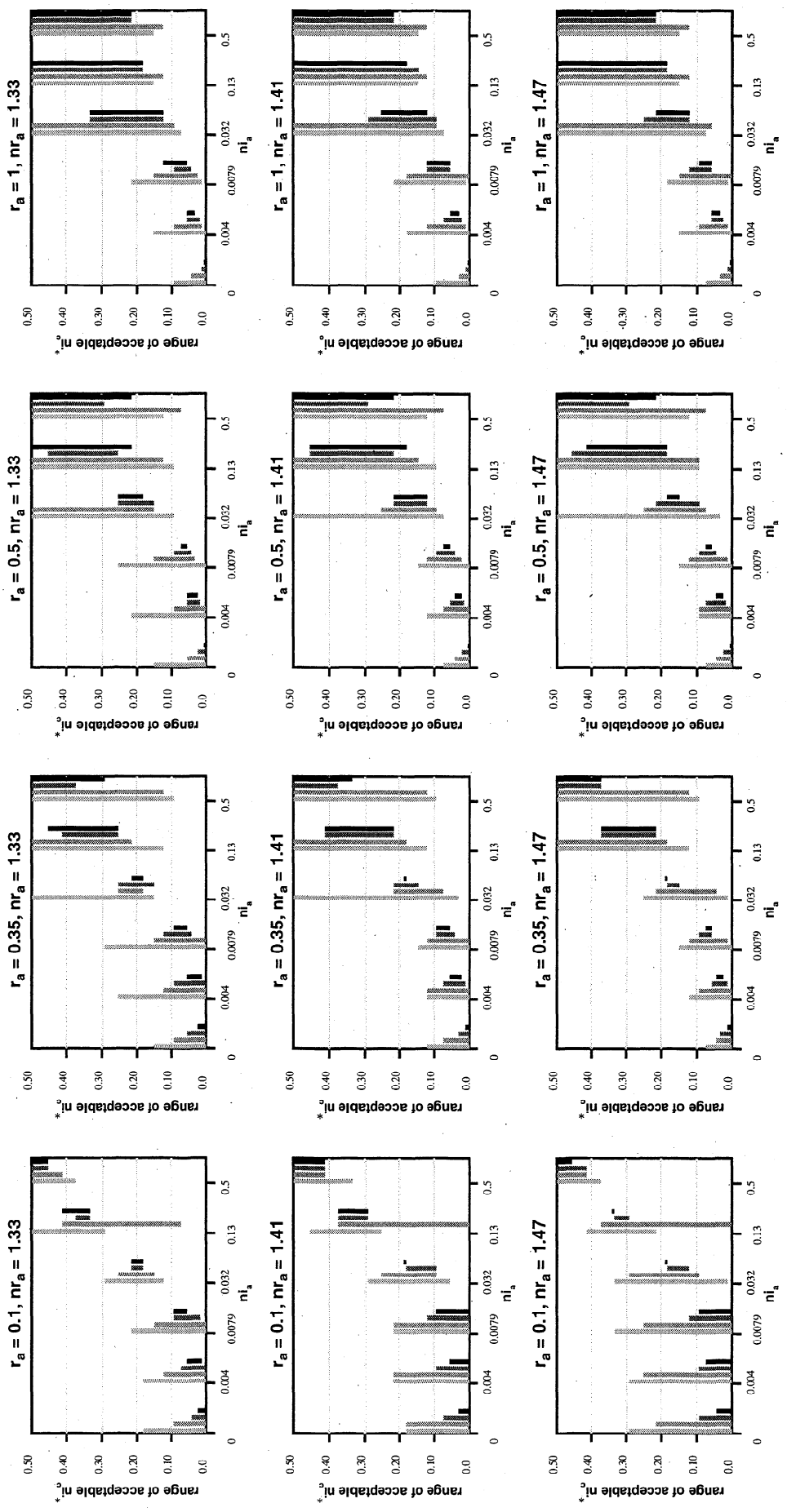

Figure 9a. Bar chart showing the ranges of particle imaginary index of refraction (ni_c) for comparison models that give acceptable matches to an atmosphere with accumulation mode particles having selected values of characteristic radius and real index of refraction. For an acceptable match, all four χ^2 test variables must fall between 0 and 2. Bars are produced for four choices of atmospheric particle imaginary index of refraction (ni_a). For each ni_a, a group of four bars is produced, corresponding to four choices of atmospheric optical depth (τ_a). As shading increases, the bars represent values of τ_a increasing from 0.05 to 0.1, 0.5, and 1.0. Note that the ordinates are scaled logarithmically. The values of ni_c at the six tick marks are 0.0, 0.0026, 0.0058, 0.0100, 0.0151, and 0.0216. The vertical axis has been scaled as $\log_{10}(1.0 + 100.0 \text{ (range of acceptable } ni_c))$.

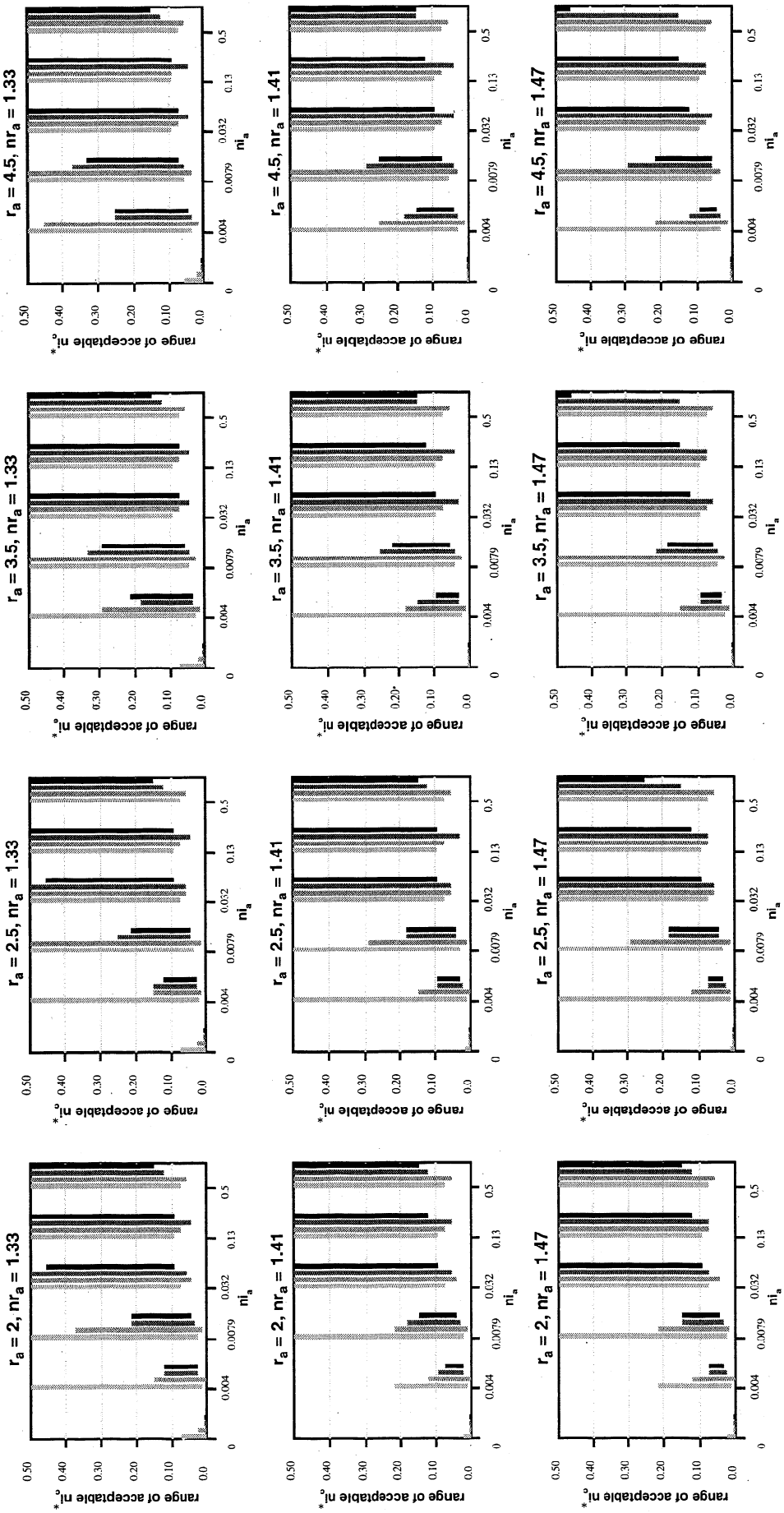

Figure 9b. Same as Figure 9a but for part of the coarse mode particle parameter space.

surface temperature (SST) data are often used: the satellite data are assimilated with in situ measurements from ships and buoys. Satellite data provide a way to "interpolate" between field measurements, giving vastly more information about global, time-varying spatial distributions. With the help of additional constraints from in situ aerosol measurements we plan to use the MISR data products for studies of global aerosol budgets.

In work currently underway, we are extending our prelaunch assessment of MISR sensitivity to deal with mixes of commonly occurring particles.

Acknowledgments. We thank our colleagues C. Bruegge and J. Martonchik for many discussions on these topics. This research is supported by the EOS-MISR instrument investigation and by the Climate and Radiation Research and Analysis Program in the Earth Sciences Division of the National Aeronautics and Space Administration, under R. Curran. This work is performed at the Jet Propulsion Laboratory, California Institute of Technology, under contract with NASA.

References

Andreae, M. O., Climatic effects of changing atmospheric aerosol levels, in *World Survey of Climatology*, vol. 16, *Future Climates of the World*, edited by A. Henderson-Sellers, pp. 341–392, Elsevier, New York, 1995.

Bevington, P. R., and D. K. Robinson, *Data Reduction and Error Analysis for the Physical Sciences*, 2nd ed., 328 pp., McGraw-Hill, New York, 1992.

Bruegge, C., N. Chrien, R. Kahn, J. Martonchik, and D. Diner, MISR radiometric uncertainty analyses and their utilization within geophysical retrievals, *IEEE Trans. Geosci. Remote Sens.*, *36*, 1186–1198, 1998.

Charlson, R. J., S. Schwartz, J. Hales, R. Cess, J. Coakley Jr., J. Hansen, and D. Hofmann, Climate forcing by anthropogenic aerosols, *Science*, *255*, 423–430, 1992.

d'Almeida, G. A., P. Koepke, and E. P. Shettle, *Atmospheric Aerosols: Global Climatology and Radiative Characteristics*, A. Deepak, Hampton, Va., 1991.

Diner, D. J., C. J. Bruegge, J. V. Martonchik, G. W. Bothwell, E. D. Danielson, E. L. Floyd, V. G. Ford, L. E. Hovland, K. L. Jones, and M. L. White, A multi-angle imaging spectroradiometer for terrestrial remote sensing from the Earth Observing System, *Int. J. Imaging Syst. Technol.*, *3*, 92–107, 1991.

Diner, D. J., W. Abdou, T. Ackerman, K. Crean, H. Gordon, R. Kahn, J. Martonchik, S. McMuldroch, S. Paradise, B. Pinty, M. Verstrete, M. Wang, and R. West, MISR level 2 aerosol retrieval algorithm theoretical basis, *Rep. JPL-D11400*, rev. C, Jet Propul. Lab., Pasadena, Calif., 1997.

Diner, D. J., et al., Multiangle imaging spectroradiometer (MISR) description and experiment overview, *IEEE Trans. Geosci. Remote Sens.*, *36*, 1072–1087, 1998.

Hanel, G., The properties of atmospheric aerosol particles as functions of relative humidity at thermodynamic equilibrium with the surrounding moist air, *Adv. Geophys.*, *19*, 73–188, 1976.

Hansen, J. E., and L. D. Travis, Light scattering in planetary atmospheres, *Space Sci. Rev.*, *16*, 527–610, 1974.

Hansen, J., M. Sato, A. Lacis, and R. Ruedy, The missing climate forcing, *Philos. Trans. R. Soc. London, Ser. B*, *352*, 231–240, 1997.

Kahn, R., R. West, D. McDonald, B. Rheingans, and M. I. Mishchenko, Sensitivity of multiangle remote sensing observations to aerosol sphericity, *J. Geophys. Res.*, *102*, 16,861–16,870, 1997.

Martonchik, J. V., D. J. Diner, R. Kahn, T. P. Ackerman, M. M. Verstraete, B. Pinty, and H. R. Gordon, Techniques for the retrieval of aerosol properties over land and ocean using multiangle data, *IEEE Trans. Geosci. Remote Sens.*, *36*, 1212–1227, 1998.

Mishchenko, M. I., W. B. Rossow, A. Macke, and A. A. Lacis, Sensitivity of cirrus cloud albedo, bidirectional reflectance, and optical thickness retrieval accuracy to ice particle shape, *J. Geophys. Res.*, *101*, 16,973–16,985, 1996.

Mishchenko, M. I., L. Travis, R. Kahn, and R. West, Modeling phase functions for dust-like tropospheric aerosols using a shape mixture of randomly oriented polydisperse spheroids, *J. Geophys. Res.*, *102*, 16,831–16,847, 1997.

Penner, J. E., R. J. Charlson, J. M. Hales, N. S. Laulainen, R. Leifer, T. Novakov, J. Ogren, L. F. Radke, S. E. Schwartz, and L. Travis, Quantifying and minimizing uncertainty of climate forcing by anthropogenic aerosols, *Bull. Am. Meteorol. Soc.*, *75*, 375–400, 1994.

Pruppacker, H. R., and J. D. Klett, *Microphysics of Clouds and Precipitation*, 714 pp., D. Reidel, Norwell, Mass., 1978.

Rao, C. R. N., L. L. Stowe, and E. P. McClain, Remote sensing of aerosols over the oceans using AVHRR data: Theory, practice and applications, *Int. J. Remote Sens.*, *10*, 743–749, 1989.

Remer, L. A., Y. J. Kaufman, B. N. Holben, A. M. Thompson, and D. McNamara, Biomass burning aerosol size distribution and modeled optical properties, *J. Geophys. Res.*, in press, 1998.

Shettle, E. P., and R. W. Fenn, Models for the aerosols of the lower atmosphere and the effects of humidity variations on their optical properties, *Tech. Rep. AFGL-TR-79-0214*, 94 pp., Air Force Geophys. Lab., Bedford, Mass., 1979.

Sokolik, I. N., and O. B. Toon, Direct radiative forcing by anthropogenic airborne mineral aerosols, *Nature*, *381*, 681–683, 1996.

Stowe, L. L., A. M. Ignatov, and R. R. Singh, Development, validation, and potential enhancements to the second-generation operational aerosol product at the National Environmental Satellite, Data, and Information Service of the National Oceanic and Atmospheric Administration, *J. Geophys. Res.*, *102*, 16,923–16,934, 1997.

Tegen, I., and A. A. Lacis, Modeling of particle size distribution and its influence on the radiative properties of mineral dust aerosol, *J. Geophys. Res.*, *101*, 19,237–19,244, 1996.

Wang, P.-H., M. P. McCormick, T. J. Swissler, M. T. Osborn, W. H. Fuller, and G. K. Yue, Inference of stratospheric aerosol composition and size distribution from SAGE II satellite measurements, *J. Geophys. Res.*, *94*, 8435–8446, 1989.

World Climate Programme WCP-112 (WCP), A preliminary cloudless standard atmosphere for radiation computation, 53 pp., Int. Assoc. for Meteorol. and Atmos. Phys., Boulder, Colo., 1984.

P. Banerjee, D. J. Diner, R. Kahn, and D. McDonald, Jet Propulsion Laboratory, MS 169-237, 4800 Oak Grove Drive, Pasadena, CA 91109. (e-mail: ralph.kahn@jpl.nasa.gov)

(Received December 16, 1997; revised April 29, 1998; accepted May 8, 1998.)